Rare Metal Materials and Engineering
Volume 54, Issue 10, October 2025
Available online at www.rmme.ac.cn

Science Press

Cite this article as: Zhang Baowei, Niu Jiajia, Zeng Zhiwei, et al. Hot Deformation Behavior and Processing Map of 23Cr-8Ni Steel[J]. Rare Metal Materials and Engineering, 2025, 54(10): 2501-2508.DOI: https://doi.org/10.12442/j.issn.1002-185X.20240514.

ARTICLE

Hot Deformation Behavior and Processing Map of 23Cr-8Ni Steel

Zhang Baowei[1], Niu Jiajia[1], Zeng Zhiwei[1], Wang Xian[1], Zhang Yuxiang[1,2], Huang Dong[1], Gao Zhenpeng[1]

[1] Luoyang Ship Material Research Institute (CSSC No.725 Institute), Luoyang 471000, China; [2] National Key Laboratory for Marine Corrosion and Protection, Qingdao 266100, China

Abstract: Using a Gleeble 3500 thermomechanical simulation testing machine, the hot deformation characteristics of 23Cr-8Ni steel were investigated under the conditions of 1000–1250 °C and 0.001–10 s^{-1}. Furthermore, the microstructure of the characterization region was analyzed to investigate the recrystallization behavior of 23Cr-8Ni steel. Results show that as the strain rate decreases and the deformation temperature increases, the flow stress decreases. Because the softening phenomenon occurs after the peak stress, the flow stress decreases. The stress index (n) is 4.28, and the thermal deformation activation energy (Q) is 588 878 J/mol. Processing map is established, and an optimal thermal processing range of 0.001–0.1 s^{-1} and 1000–1200 °C is achieved, therefore greatly promoting the yield rate.

Key words: hot deformation behavior; processing map; 23Cr-8Ni steel; GLEEBEL 3500

1 Introduction

Because of its superior mechanical qualities, strong corrosion resistance, and reasonable cost, high-nitrogen (N) austenitic stainless steel, which is prepared by partially or completely substituting N for nickel (Ni), has been used extensively in various fields, such as manufacturing, biomedical engineering, and ocean engineering[1]. N also has numerous positive effects on austenitic stainless steels. By preventing the δ-ferrite growth at high temperatures during deformation, austenite can be stabilized. In addition to other alloying elements, N not only enhances the yield strength of austenite, but also improves the resistance against corrosion, stress corrosion, and creep[2]. 23Cr-8Ni steel is a novel type of high-strength, high-N austenitic stainless steel, and its yield strength is greater than 600 MPa. 23Cr-8Ni steel is nonmagnetic, so it can be used in nonmagnetic machinery.

The hot processing map of metal materials has been widely researched. Fu et al[3] established a hot processing map, analyzed the work hardening mechanism of 0Cr11Ni2MoVNb stainless steel, and then proposed the optimal temperature and strain rate ranges for hot ring rolling. Wu et al[4] investigated the intrinsic connection between the flow stress and deformation behavior of Gh4065A nickel-based superalloy. Two instability domains were divided. In addition, the instability mechanism of these two domains was discussed. Lu et al[5] analyzed the high temperature deformation behavior of TC11 with coarse lamellar starting microstructure. The deformation mechanisms of the alloy processed according to the optimized hot compression process windows were identified as spheroidizing and dynamic recrystallizing controlled by the self-diffusion mechanism. Liu et al[6] evaluated the deformation characteristics of as-cast S31254 super-austenitic stainless steel by isothermal compression testing, and the safe deformation domain was identified from the processing map. Meanwhile, three unstable regions should be avoided in hot processing. Flow stress during the hot deformation process and processing map for 316LN steel were investigated[7]. Both the constitutive equation and processing map for 316LN steel were obtained, and the optimal hot-working condition for 316LN was confirmed. Guan et al[8] studied the hot deformation behavior of as-cast

Received date: October 13, 2024
Corresponding author: Zhang Baowei, Master, Senior Engineer, Luoyang Ship Material Research Institute (CSSC No. 725 Institute), Luoyang 471000, P. R. China, Tel: 0086-379-67256402, E-mail: zhangbaowei@725.com.cn

CoNi-based superalloy and reported that the predominant recrystallization mechanism during hot working was discontinuous dynamic recrystallization (DRX), which was related to strain-induced grain boundary migration. Meanwhile, subgrains formed around *M*C carbides and shear bands, which contributed to DRX. Furthermore, fine γ' precipitates slowed down the recrystallization process. The true stress-true strain curves of GH901 superalloy under various deformation conditions were obtained via thermal compression experiments. Processing maps were established for the GH901 superalloy using the strain compensation and strain of 0.3. These results demonstrated a relationship among the true strains, temperatures, strain rates, and deformation behavior of the GH901 superalloy[9]. Superalloys have a well-documented processing map and hot deformation behavior[10–18]. However, the thermomechanical processing and high-N austenitic stainless steel processing maps are rarely reported.

23Cr-8Ni steel is still being developed. Although there are many alloying elements, their effect on the hot workability is normally inferior. During forging and rolling procedures, there are usually several problems, such as surface cracking and coarse grains, and the yield rate is only about 50%. The setting of the hot working process is usually based on experience instead of a theoretical basis. Additionally, the hot working process has rarely been developed, which harms ultrasonic inspection and further processing[19].

Temperature T and strain rate $\dot{\varepsilon}$ can be optimized using a dynamic material mode (DMM)-based processing map. It also provides useful information and theoretical support for plastic processing procedures. A multitude of constitutive models based on metal materials have been developed in recent years to describe the high-temperature deformation properties of alloys, including Arrhenius model, Johnson-Cook (J-C) model, and Zerelli-Armstrong (Z-A) model.

In this research, the thermomechanical process parameters were investigated for the production of flawless hot-worked goods. The effects of temperature and strain rate on the deformation characteristics of 23Cr-8Ni steel were analyzed to obtain the deformation processing maps, and the constitutive equation of 23Cr-8Ni steel was achieved. Furthermore, the microstructures were examined to validate the deformation mechanism.

2 Experiment

To melt the 23Cr-8Ni steel, industrial pure primary materials, such as chromium, nickel plates, and molybdenum bars, were used in an intermediate-frequency furnace for electroslag remelting. Table 1 displays the chemical composition of 23Cr-8Ni steel.

By applying a Gleeble 3500 thermomechanical simulation testing machine, high-temperature deformation experiments were performed at 1000–1250 °C with uniform strain rates of 10^{-3} – 10 s^{-1}. The dimension of the cylindrical deformation sample was Φ10 mm×15 mm, and the sheets of tantalum and graphite were positioned between the ends of the sample and the anvil along with the Ni lubricant. Adequate lubricant was provided during each experiment to minimize friction and prevent the sample and anvil from bonding together at high temperatures[20–21].

To achieve a consistent temperature distribution over the sample, all samples were heated at heating rate of 10°/s to the test temperature and held for 5 min. After the samples were deformed to 50% reduction in height, they were quenched for microstructure observation. Fig. 1 depicts the hot deformation (compression) test process for 23Cr-8Ni steel, and Fig. 2 shows the appearances of the sample before and after compression deformation.

Microstructure observation of the deformed samples was performed on cross-sections that were cut parallel to the compression axis. The microstructure of the cross-sections was observed by OLYMPUS GX71 metallographic microscope after erosion by aqua regia. FEI Scios2 compact field emission scanning electron microscope coupled with electron backscatter diffraction (EBSD) detector was used at operating voltage of 20 kV with scanning step of 0.3 μm.

Fig. 3 shows the initial metallographic structure of the 23Cr-8Ni steel before deformation. The matrix is composed of only one phase of austenite structure with some twinning structures.

Table 1 Chemical composition of 23Cr-8Ni steel (wt%)

Cr	Ni	Mn	Mo	N	C	Fe
23.0	12.1	10.2	3.2	0.7	0.02	50.6

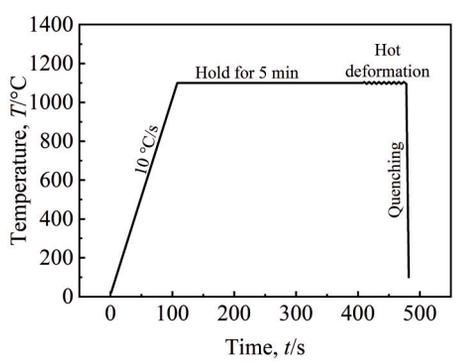

Fig.1 Schematic diagram of hot deformation process

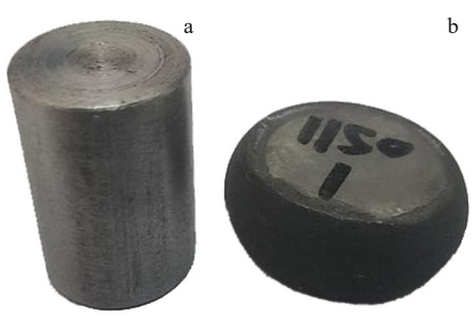

Fig.2 Appearances of sample before (a) and after (b) compression deformation

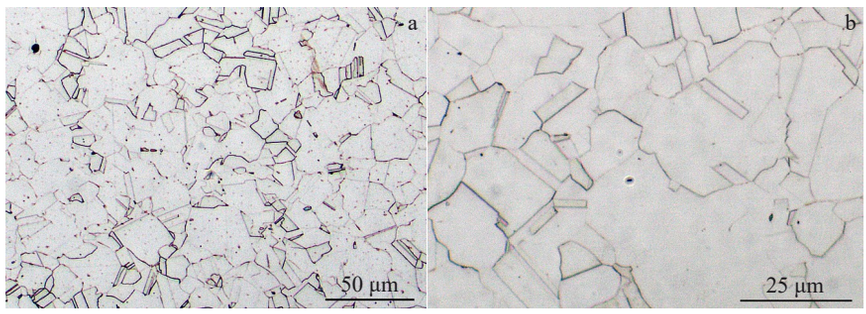

Fig.3 Initial metallographic structures of 23Cr-8Ni steel

3 Results and Discussion

3.1 True stress-true strain analysis

Fig. 4 displays the flow behavior of 23Cr-8Ni steel. Every true stress-true strain curve has a peak stress. Based on the position of peak stress occurrence, the true stress-true strain curve can be divided into two phases. The work hardening caused by tangles and dislocation reproduction causes the rapid increase in flow stress during the first stage of deformation. The dynamic recovery (DRV) softening effect is not obvious. The softening effect is strengthened when the deformation degree increases, leading to DRX at a critical strain. The peak stress appears when the work hardening and dynamic softening reach an equilibrium state. Because of the decreasing dislocation density and DRX degree in the second stage, the flow stress decreases as the strain increases. This is because work hardening is subordinated to the softening effect, which encompasses both DRV and DRX. True stress-true strain curves usually have DRX features with a prominent peak stress due to the balance state between dynamic softening and work hardening. The flow stress is increased with the decrease in temperature and the increase in strain rate.

3.2 Effect of deformation temperature on microstructure

Fig.5a and 5b display the microstructures of 23Cr-8Ni steel at strain rate of 0.1 s^{-1} and deformation temperatures of 1000 and 1250 °C, respectively. When the deformation temperature is 1000 °C, the microstructures are composed of tiny DRX grains with size ranging from 1 μm to 5 μm. Some deformed grains have not undergone recrystallization. When the deformation temperature reaches 1250 °C, the grains develop dramatically as a result of the temperature increase, and the majority of the grains become coarse with the size of approximately 50 μm. This phenomenon demonstrates that the deformation temperature has a major effect on both the grain size and DRX during the deformation process.

3.3 Effect of strain rate on microstructure

The microstructures of the 23Cr-8Ni steel at deformation

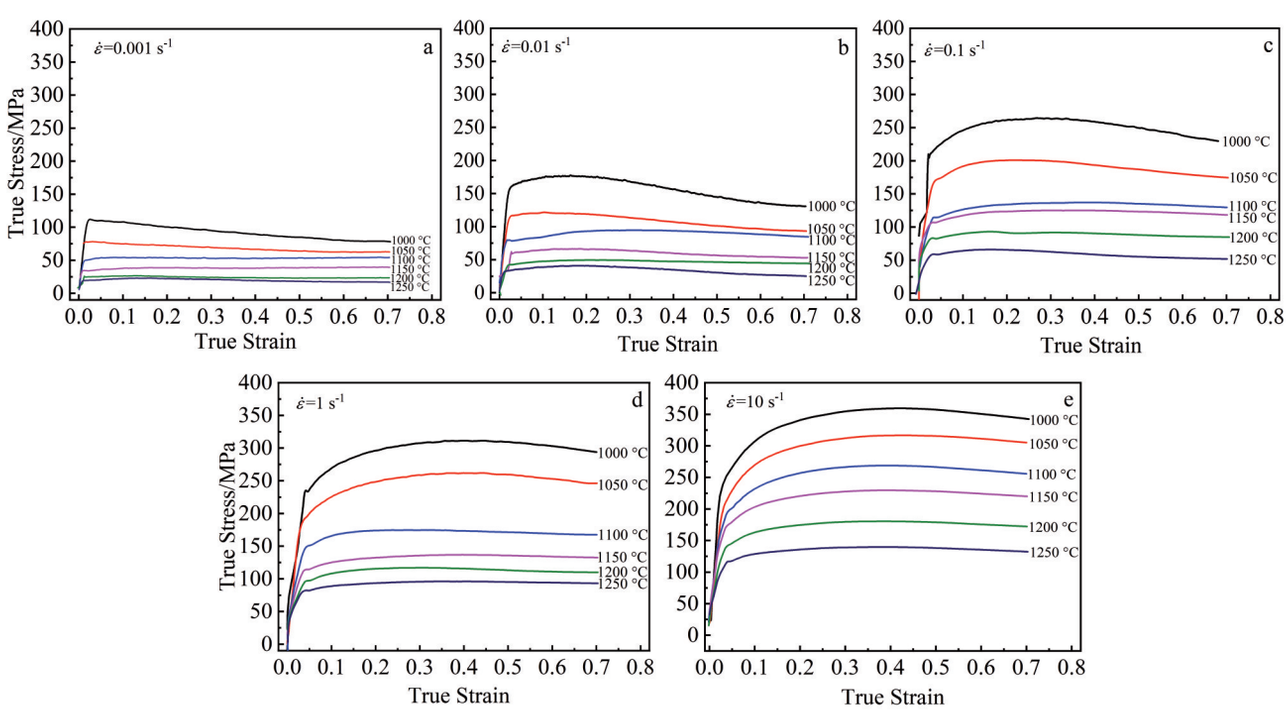

Fig.4 True stress-true strain curves of 23Cr-8Ni steel at different temperatures and different strain rates: (a) $\dot{\varepsilon}$=0.001 s^{-1}, (b) $\dot{\varepsilon}$=0.01 s^{-1}, (c) $\dot{\varepsilon}$= 0.1 s^{-1}, (d) $\dot{\varepsilon}$=1 s^{-1}, and (e) $\dot{\varepsilon}$=10 s^{-1}

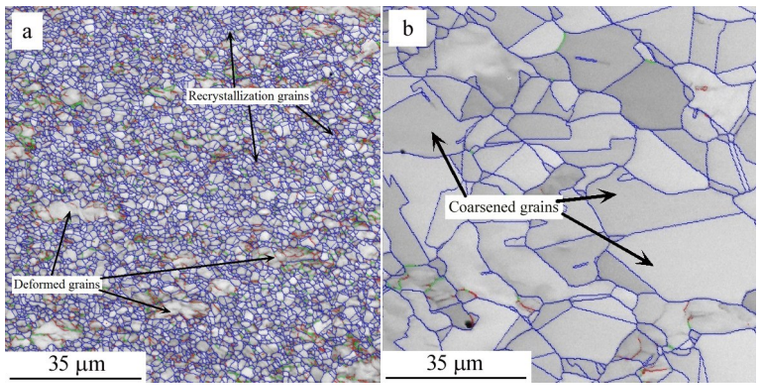

Fig.5 Microstructures of 23Cr-8Ni steel at strain rate of 0.1 s^{-1} and deformation temperature of 1000 °C (a) and 1250 °C (b)

temperature of 1100 °C and different strain rates are shown in Fig.6. As shown in Fig.6a, there are large deformed grains and small equiaxed grains. The small equiaxed grains should be considered as recrystallized grains. The metal atoms can fully diffuse, which encourages the nucleation and complete development of DRX due to the strain rate of 0.001 s^{-1}, which indicates the sufficient deformation time of approximately 15.3 min. It is almost impossible to obtain homogenous and completely recrystallized grains at strain rate of 10 s^{-1} due to the too short deformation time (0.09 s). The elongated distorted grains still exist, as shown in Fig.6b, and almost no recrystallized grains can be observed.

3.4 Constitutive analysis

The common model for assessing and forecasting deformation flow behavior is the Arrhenius model[22–24]. To further clarify the connection between predicted flow stress and experiment results of thermal compression, the relationship between T and $\dot{\varepsilon}$ is described by the Arrhenius model, and the constitutive equations of $\dot{\varepsilon}$ are represented by Eq.(1–3)[25], as follows:

$$\dot{\varepsilon} = A_1\sigma^{n_1}\exp\left(-\frac{Q}{RT}\right) \quad (1)$$

$$\dot{\varepsilon} = A_2\exp(\beta\sigma)\exp\left(-\frac{Q}{RT}\right) \quad (2)$$

$$\dot{\varepsilon} = A\left[\sinh(\alpha\sigma_p)\right]^n\exp\left(-\frac{Q}{RT}\right) \quad (3)$$

where n and n_1 are referred to as the stress exponents; A_1 and A_2 are material characteristics associated with the strain rate-sensitive parameter; R is the gas constant; Q is thermal deformation activation energy; σ is flow stress; σ_p is peak stress; A, α, and β are model parameters. According to Ref. [26–28], several variables are defined, as expressed by Eq.(4–8):

$$\alpha=\beta/n_1 \quad (4)$$

$$Z=\dot{\varepsilon}\exp\left(-\frac{Q}{RT}\right) \quad (5)$$

$$\ln\dot{\varepsilon} = \ln A_1 + n_1\ln\sigma - \frac{Q}{RT} \quad (6)$$

$$\ln\dot{\varepsilon} = \ln A_2 + \beta\sigma - \frac{Q}{RT} \quad (7)$$

$$\ln\dot{\varepsilon} = \ln A + n\ln\left[\sinh(\alpha\sigma_p)\right] - \frac{Q}{RT} \quad (8)$$

The constitutive model was established using the peak stress data under various deformation conditions, as listed in Table 2.

In the analysis, $\ln\sigma_p$ is used as the X axis, and $\ln\dot{\varepsilon}$ is used as the Y axis, as depicted in Fig.7a. Similarly, σ_p is utilized as the X axis, and $\ln\dot{\varepsilon}$ is used as the Y axis, as shown in Fig. 7b. Subsequently, to determine the slope of fitting lines at different deformation temperatures, linear regression is used for analysis. The average values of n_1 and β are 6.1662 and 0.048 MPa^{-1}, respectively. Using these values, the parameter α

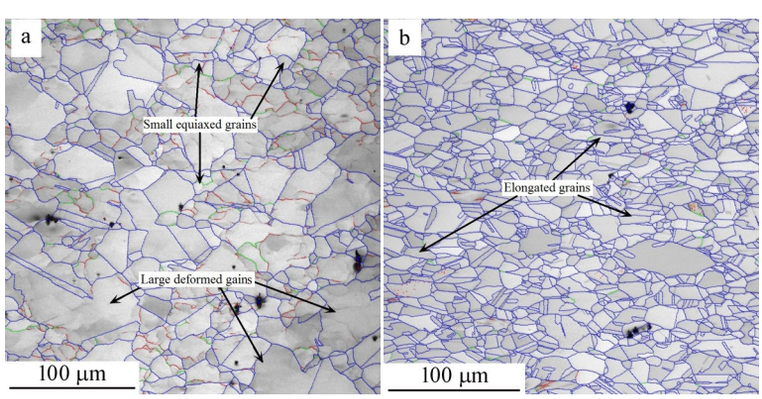

Fig.6 Microstructures of 23Cr-8Ni steel at deformation temperature of 1100 °C and strain rate of 0.001 s^{-1} (a) and 10 s^{-1} (b)

Table 2 Peak stress under different deformation temperatures and strain rates (MPa)

Strain rate/s^{-1}	Deformation temperature/°C					
	1000	1050	1100	1150	1200	1250
10	360.0	317.0	268.0	230.0	180.0	140.0
1	312.0	262.0	175.0	137.0	128.0	96.0
0.1	265.0	201.0	137.0	87.0	94.0	66.5
0.01	178.0	121.0	99.0	66.0	52.0	41.0
0.001	112.0	78.0	54.0	40.0	26.5	23.0

is calculated as 0.0078 MPa^{-1}. Fig.7c shows the fitting lines of $\ln[\sinh(\alpha\sigma_p)]$ -$\ln\dot{\varepsilon}$, and the line slope is obtained by linear regression. Consequently, the average value of n is 4.28.

By calculating the partial derivative of Eq. (3), the activation energy Q may be expressed by Eq.(9), as follows:

$$Q=R\left|\frac{\partial\ln\dot{\varepsilon}}{\partial\ln\left[\sinh(\alpha\sigma)\right]}\right|_T\left|\frac{\partial\ln\left[\sinh(\alpha\sigma)\right]}{\partial(1/T)}\right|_{\dot{\varepsilon}} \tag{9}$$

Fig. 7d shows that the relationship between $\ln[\sinh(\alpha\sigma_p)]$ and T^{-1} is completely linear. Thus, the activation energy of 23Cr-8Ni steel is 588 878 J/mol.

Substitute the calculated parameter values into Eq.(8), and the value of parameter A is obtained as $e^{46.4}$. Based on Eq.(4), the peak stress of 23Cr-8Ni steel can be obtained by Eq.(10), as follows:

$$\dot{\varepsilon}=e^{46.4}\left[\sinh\left(0.0078\sigma_p\right)\right]^{4.28}\exp\left(-\frac{588878}{8.314T}\right) \tag{10}$$

To confirm the accuracy of Eq.(10), the experiment data are compared with the predicted peak stress under different conditions. As shown in Fig. 8, the difference is relatively small between the predicted and experimental peak stresses, and the maximum deviation is only 15 MPa, suggesting a high accuracy of the constitutive equation.

3.5 Establishment of processing map

Eq.(11) can be used to determine the dissipation power (P) based on DMM, as follows:

$$P=\sigma\dot{\varepsilon}=G+J=\int_0^{\dot{\varepsilon}}\sigma\mathrm{d}\dot{\varepsilon}+\int_0^{\sigma}\dot{\varepsilon}\mathrm{d}\sigma \tag{11}$$

with

$$\sigma=K(\dot{\varepsilon})^m \tag{12}$$

$$m=\frac{\mathrm{d}J}{\mathrm{d}G}=\frac{\dot{\varepsilon}\partial\sigma}{\sigma\partial\dot{\varepsilon}}=\frac{\partial(\ln\sigma)}{\partial(\ln\dot{\varepsilon})} \tag{13}$$

$$J=\int_0^{\sigma}\dot{\varepsilon}\mathrm{d}\sigma=\frac{m}{m+1}\dot{\varepsilon}\sigma \tag{14}$$

where G and J are portions of P; m is the strain rate sensitivity; K is a constant. Therefore, the power dissipation efficiency η is introduced to assess the power-dissipation capacity and can be expressed by Eq.(15), as follows:

$$\eta=\frac{J}{J_{\max}}=\frac{2m}{m+1} \tag{15}$$

To further investigate the effect of strain rate on the plastic formation, Chen et al[29] proposed an instability zone of plastic deformation in terms of the instability parameter ξ, as expressed by Eq.(16):

$$\xi(\dot{\varepsilon})=\frac{\partial\ln\left(\frac{m}{m+1}\right)}{\partial\ln\dot{\varepsilon}}+m \tag{16}$$

The processing area with ξ<0 is identified as the instability domain, and the remaining portion is considered the safe domain. The cubic polynomial of η is determined in relation

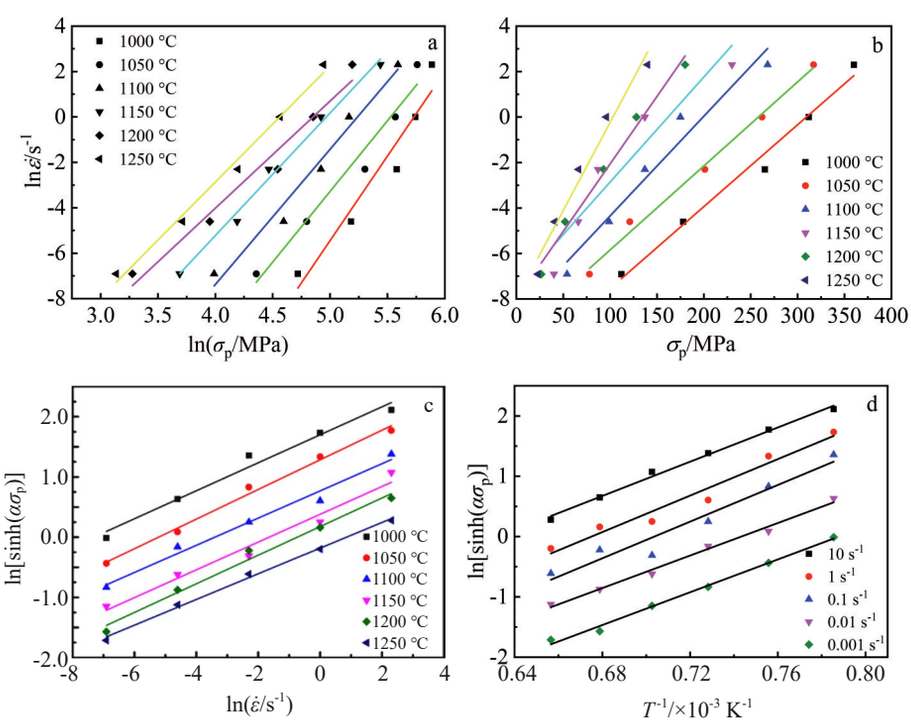

Fig.7 Linear fitting results between different variables: (a) $\ln\dot{\varepsilon}$-$\ln\sigma_p$; (b) $\ln\dot{\varepsilon}$-σ_p; (c) $\ln[\sinh(\alpha\sigma_p)]$-$\ln\dot{\varepsilon}$; (d) $\ln[\sinh(\alpha\sigma_p)]$-$T^{-1}$

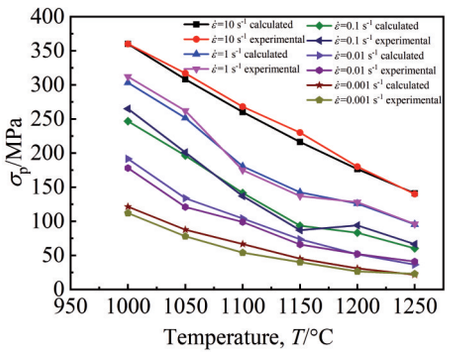

Fig.8 Comparison of calculated and experimental peak stresses under different conditions

to ln$\dot{\varepsilon}$, as follows:

$$\ln\left(\frac{m}{m+1}\right)=a+b\ln\dot{\varepsilon}+c(\ln\dot{\varepsilon})^2+d(\ln\dot{\varepsilon})^3 \quad (17)$$

Typically, a power dissipation map and an instability map are coupled to form a hot processing map and then to illustrate the flow instability restrictions and microstructure evolutions. The shaded region indicates the dominance of flow instability. As a result, a particular mechanism for lowering energy usage can be found. Higher power dissipation efficiencies are generally associated with improved workability unless they encounter unreliable changes, such as unanticipated fracture. Therefore, the goal of microstructure optimization can be achieved by selecting the working parameters with the maximum efficiency.

Fig. 9 displays the hot processing maps of 23Cr-8Ni steel under different true strains. The safety zone is represented by the white area, whereas the instability region is represented by the gray area (ξ<0). As shown in Fig. 9, there is an instability region in the low-temperature and intermediate-strain rate area (1000–1050 °C, 0.01–1 s^{-1}) when the true strain is 0.2. The instability region expands dramatically when the true strain increases to 0.7. The instability region changes from 1000–1170 °C and 0.1–10 s^{-1} to 1230–1250 °C and 5–10 s^{-1}. The optimal forging parameters are in the zone with higher power dissipation values away from the unstable area. The ideal processing range for 23Cr-8Ni steel is 1000–1200 °C and 10^{-3}–10^{-1} s^{-1} when the true strain is 0.7. The yield rate of 23Cr-8Ni steel increases from 50% to over 85% when these processing parameters are selected for production.

3.6 Microstructure evolution

It is widely acknowledged that there are several microstructure mechanisms for the domains crucial to the power dissipation efficiency[30–31]. A thorough discussion of each zone of the produced processing maps is conducted to examine the microstructure evolution. Take the hot processing map in Fig.9f as an example. It can be seen that area B is an unstable region with high temperatures; area A is an unstable region with η value between 0.16 and 0.24; area C with η of 0.31–0.48 is a safe area. The microstructures of these three areas are characterized by EBSD, as displayed in Fig.10. Fig.10a shows the microstructure under conditions of 1050 °C and 1 s^{-1}. It is observed that a majority of grains are deformed, and small equiaxed grains appear at the initial grain boundaries, which indicates that recrystallization occurs. The proportion of DRX can be calculated by the misorientation profiles. Fig. 10b shows the distribution of recrystallization, where blue represents the fully recrystallized area, yellow represents the partially recrystallized area, and red represents the unrecrystallized area. The volume fraction of unrecrystallized area, fully recrystallized area, and partially recrystallized area is 63.4%, 12.6%, and 23.7%, respectively. Fig. 10c shows the distribution of recrystallization under conditions of 1000 °C

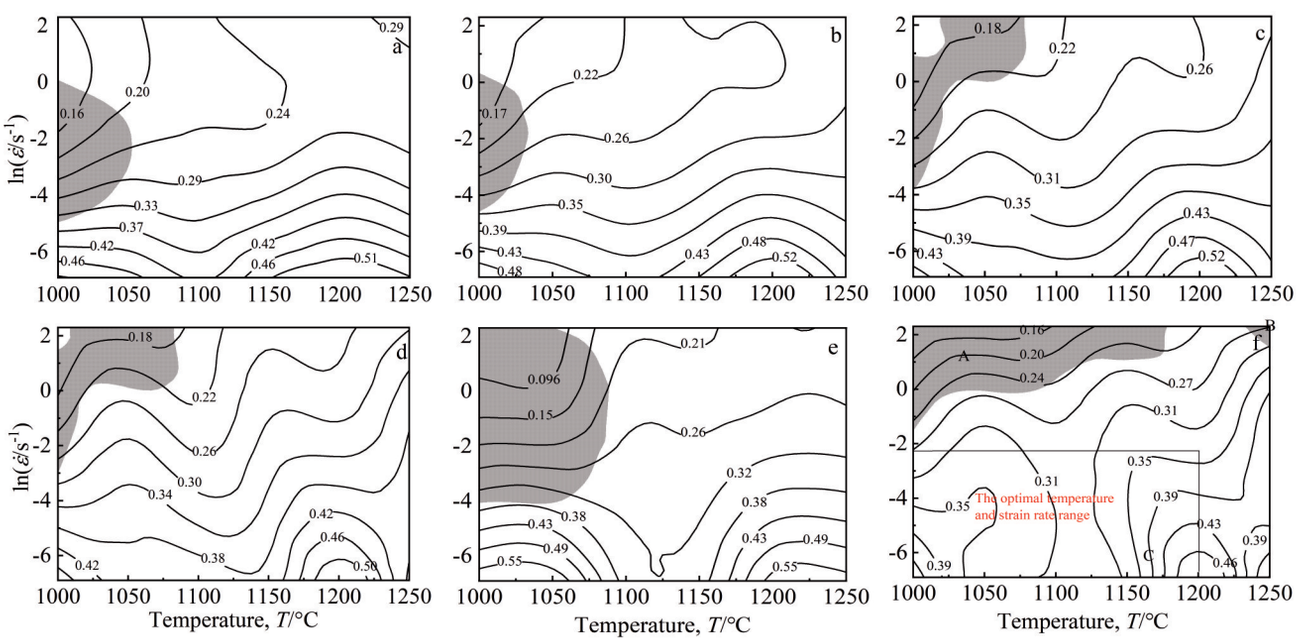

Fig.9 Hot processing maps of 23Cr-8Ni steel under true strain of 0.2 (a), 0.3 (b), 0.4 (c), 0.5 (d), 0.6 (e), and 0.7 (f)

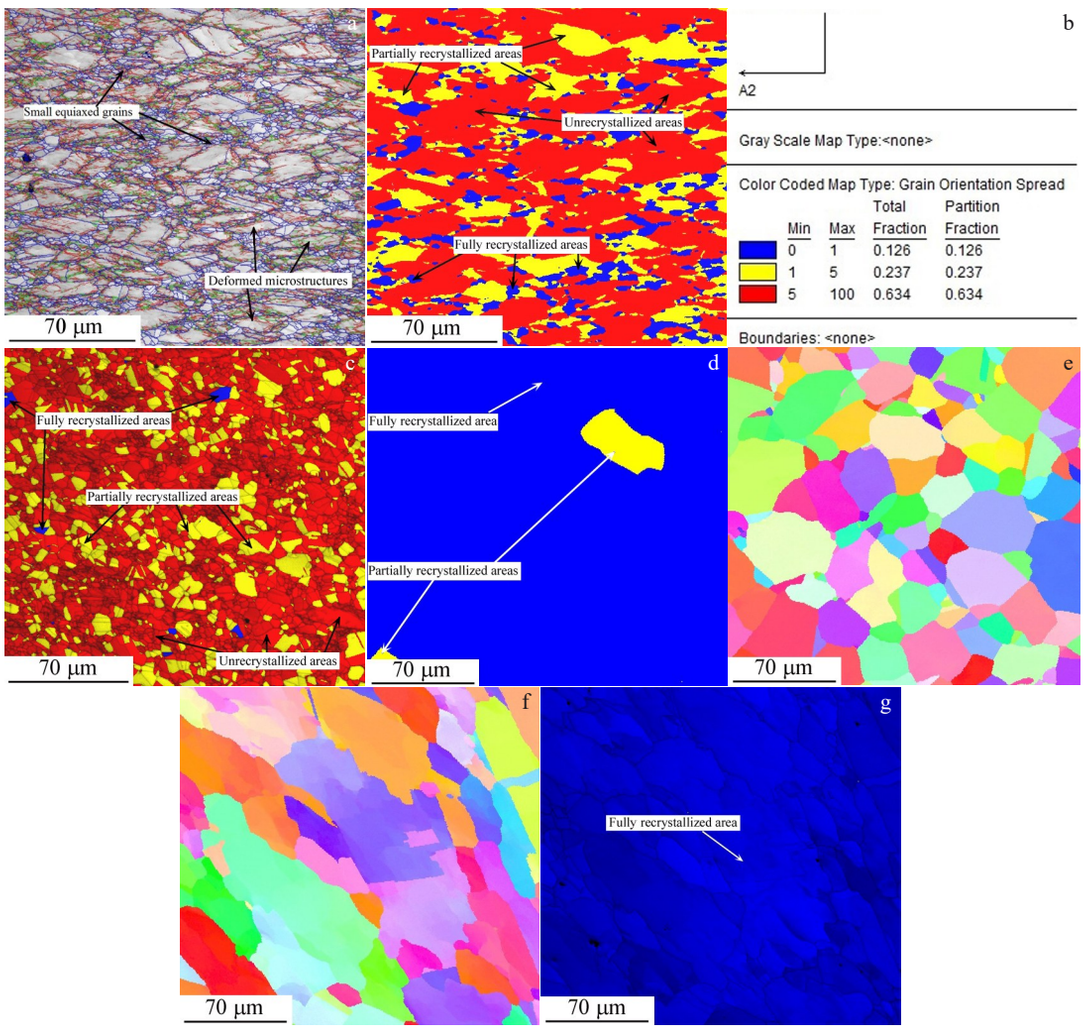

Fig.10 EBSD analysis results of area A (a–c), area B (d–e), and area C (f–g) in Fig.9f

and 1 s^{-1}. Due to the temperature decrement of 50 °C, only about 7.6% of the area undergoes complete recrystallization, and the volume fraction of unrecrystallized area increases to 75.8%. Thus, the peak stress increases from 262 MPa to 312 MPa. Under the conditions of 1250 °C and 10 s^{-1}, almost all regions undergo complete recrystallization (99.3%), the microstructure consists of coarse equiaxed grains, and no deformed grains can be observed, indicating that high temperature causes nucleation and growth of grains again after compression. Because 1250 °C is close to the melting point, the bonding force between grain boundaries weakens, and the elongation during the tensile test is almost zero. Therefore, area B is also an unstable region. Other researchers have also noted this phenomenon in various materials, including TC21 titanium alloy and 7075 aluminum alloy[32–33].

As shown in Fig. 10f, the gains are coarse and elongated, possibly due to sufficient compression time. The grains undergo both deformation and recrystallization. Fig. 10g illustrates that the recrystallization occurs in all regions. DRX plays an important role in refining grains and improving microstructures during hot deformation. DRX is believed to be the prevalent softening mechanism. The conditions of 1200 °C and 0.001 s^{-1} are typical hot working conditions in area C in Fig. 9f, where η is greater than 0.46 and also the maximum value in the hot processing map with true strain=0.7. High η indicates that the material can effectively convert external energy into plastic deformation and has good plasticity and deformation capacity under certain hot processing conditions[34–35].

4 Conclusions

1) The constitutive equation of 23Cr-8Ni steel is determined as $\dot{\varepsilon} = e^{46.4}\left[\sinh\left(0.0078\sigma_p\right)\right]^{4.28}\exp\left(-\frac{588878}{8.314T}\right)$.

2) The true stress-true strain curve shows obvious work hardening and flow softening characteristics. The flow stress is increased with the decrease in temperature and the increase in strain rate.

3) The optimal thermomechanical processing parameters are deformation temperatures of 1000–1200 °C and strain rate of 0.001–0.1 s^{-1}. With the processing parameters, the yield rate of 23Cr-8Ni steel is greatly improved.

References

1 Zhou R, Derek O N, Liu C. *Journal of Materials Research and Technology*[J], 2020, 9:1856

2 Ilola R, Hänninen H, Kauppi T. *Journal of Materials Engineering and Performance*[J], 1998, 7: 661

3 Fu J, Li F G, Li Y T. *Materials Science and Engineering A*[J], 2018, 382(2): 022027

4 Wu Jinjiang, Zhao Guangdi, Wang Bo *et al*. *Materials China*[J], 2024, 43(10): 902 (in Chinese)

5 Lu S Q, Li X, Wang K L *et al*. *Transactions of Nonferrous Metals Society of China*[J], 2013, 23(2): 353

6 Liu G W, Han Y, Shi Z Q *et al*. *Materials and Design*[J], 2014, 53: 662

7 Guo B F, Ji H P, Liu X G *et al*. *Journal of Materials Engineering and Performance*[J], 2012, 21: 1455

8 Guan Y, Liu Y C, Ma Z Q *et al*. *Metals and Materials International*[J], 2022, 8: 1488

9 Ma R, Li L L, Zhai R X *et al*. *Metals*[J], 2021, 11(11): 1808

10 Fan J K, Kou H C, Lai M J *et al*. *Materials and Design*[J], 2013, 49: 945

11 Indrani S, Ravi S K, Ramamurty U. *Materials Science and Engineering A*[J], 2010, 527: 6157

12 Jabbari-Taleghani M A, Torralba J M. *Journal of Alloys and Compounds*[J], 2014, 595: 1

13 Ning Y Q, Yao Z K, Yang Z *et al*. *Materials Science and Engineering A*[J], 2012, 531: 91

14 Wang Y, Zhen L, Shao W Z *et al*. *Journal of Alloys and Compounds*[J], 2009, 474: 341

15 Narayana M S V S, Nageswara R, Kashyap B P. *International Journal of Powder Metallurgy*[J], 2001, 44:267

16 Chen X M, Lin Y C, Wen D X *et al*. *Materials and Design*[J], 2014, 57: 568

17 Wu G C, Lin Y C, Chen M S *et al*. *Journal of Alloys and Compounds*[J], 2024, 1002: 175293

18 Lin Y C, Wu X Y, Chen X M *et al*. *Journal of Alloys and Compounds*[J], 2015, 640: 101

19 Wang Z H, Fu W T, Sun S H. *Metallurgical and Materials Transactions A*[J], 2010, 41: 1025

20 Sajadifar S V, Ketabchi M, Nourani M. *Steel Research International*[J], 2011, 82(8): 934

21 Kartika Ika, Li Yunping, Matsumoto Hiroaki *et al*. *Materials Transactions*[J], 2009, 50(9): 2277

22 Liao Q Y, Jiang Y C, Le Q C *et al*. *Journal of Materials Science and Technology*[J], 2021, 61: 1

23 Wang D X, Zhu Q Q, Wei Z X *et al*. *Journal of Alloys and Compounds*[J], 2022, 908: 164595

24 Masahiko Nishijima, Kenji Hiraga. *Materials Transactions*[J], 2007, 48(1): 10

25 Cai J, Li F G, Liu T Y *et al*. *Materials and Design*[J], 2011, 32(3): 1144

26 Mirzadeh H, Cabrera J M, Prado J M *et al*. *Materials Science and Engineering A*[J], 2011, 528: 3876

27 Scott C S, Alan A, Luo S. *Journal of Magnesium and Alloys*[J], 2020, 8(1): 111

28 Gui Y W, Ouyang L X, Xue Y B *et al*. *Journal of Materials Science and Technology*[J], 2021, 90: 205

29 Chen G X, Lu X Y, Yan J *et al*. *Metals*[J], 2022, 12(4): 541

30 Srinivasan N, Prasad Y V R K. *Metallurgical and Materials Transactions A*[J], 1994, 25: 2275

31 Ning Y Q, Yao Z K, Li H *et al*. *Materials Science and Engineering A*[J], 2010, 527: 961

32 Guo L G , Yan S, Yang H *et al*. *Chinese Journal of Aeronautics*[J], 2015, 28(6): 1774

33 Zhu Y C, Zeng W D, Feng F *et al*. *Materials Science and Engineering A*[J]2011, 528: 1757

34 Li H M, Zhang J L, Mao X N *et al*. *Rare Metal Materials and Engineering*[J], 2021, 50(6): 1980

35 Wang Fa, Jiang He, Dong Jianxin. *Rare Metal Materials and Engineering*[J], 2023, 52(1): 245 (in Chinese)

23Cr-8Ni钢热变形行为及工艺图

张宝伟[1]，牛佳佳[1]，曾志伟[1]，王　宪[1]，张玉祥[1,2]，黄　冬[1]，高珍鹏[1]

(1. 洛阳船舶材料研究所(中国船舶集团有限公司第七二五研究所)，河南 洛阳 471000)

(2. 海洋腐蚀与防护全国重点实验室，山东 青岛 266100)

摘　要：采用Gleeble 3500热力模拟试验机，研究了23Cr-8Ni钢在1000~1250 ℃和0.001~10 s^{-1}条件内的热变形行为。分析了表征区域的微观结构，研究了23Cr-8Ni钢的再结晶行为。结果表明：随着应变的降低和变形温度的升高，流变应力明显减小。由于峰值应力之后出现软化现象，流变应力减小。应力指数（n）为4.28，热变形活化能（Q）为588 878 J/mol。构建了热工艺图，获得了最佳热加工范围为0.001~0.1 s^{-1}和1000~1200 ℃。采用最佳热加工工艺，成品率大大提高。

关键词：热变形行为；工艺图；23Cr-8Ni钢；Gleebel 3500

作者简介：张宝伟，男，1977年生，硕士，高级工程师，洛阳船舶材料研究所(中国船舶集团有限公司第七二五研究所)，河南 洛阳 471000，电话：0379-67256402，E-mail：2741724909@qq.com